Supporting Information

Flexible In-Ga-Zn-N-O synaptic transistor for ultralow-power neuromorphic computing and EEG-based brain-computer interfaces

Shuangqing Fan[a†], Enxiu Wu[b†], Minghui Cao[a], Ting Xu[b], Tong Liu[b], Lijun Yang[c,*], Jie Su[a,*], Jing Liu[b,*]

[a]College of Electronics and Information, Qingdao University, Qingdao 266071, China.
[b]State Key Laboratory of Precision Measurement Technology and Instruments, School of Precision Instruments and Opto-electronics Engineering, Tianjin University, No. 92 Weijin Road, Tianjin 300072, China.
*Corresponding author email: jingliu_1112@tju.edu.cn; jsu@qdu.edu.cn; yanglijun@irm-cams.ac.cn
[†]These authors contributed equally to this work.

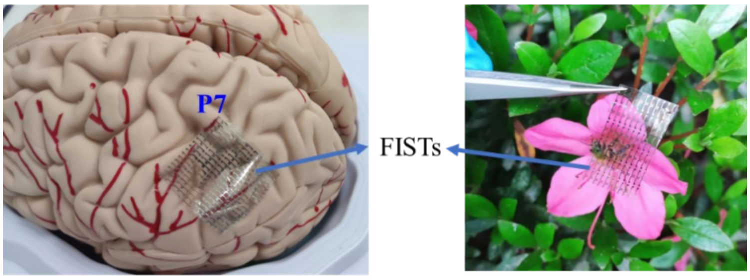

Fig. S1. Photograph of the flexible IGZNO synapse transistor array based on PET substrates with high transparency, indicating great conformability to a human brain model.

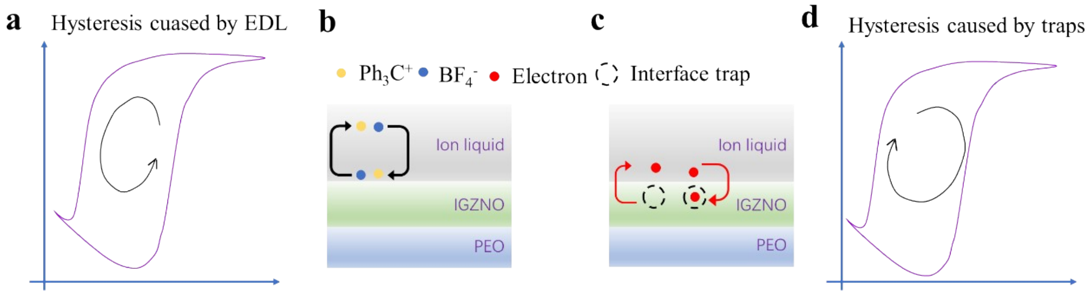

Fig. S2. Schematic illustrations of hysteresis caused by electric double layer (EDL) in the anticlockwise direction (a,b) and by interface trap in the clockwise direction (c,d).

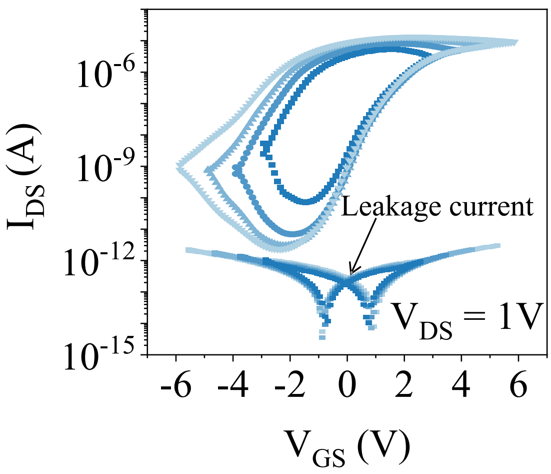

Fig. S3. The transfer characteristics and leakage current of the device were measured while sweeping the gate voltage from ±3 V to ±6 V.

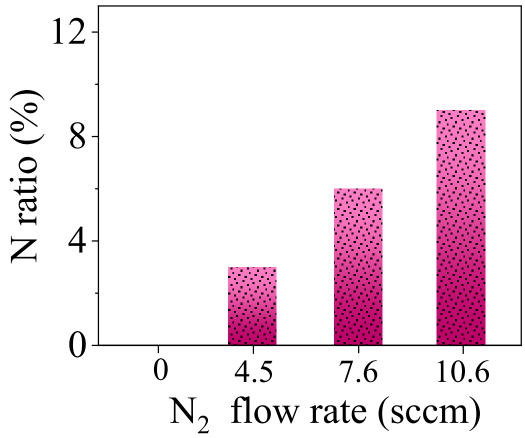

Fig. S4. Measured atomic ratio of IGZNO film under different nitrogen gas streams.

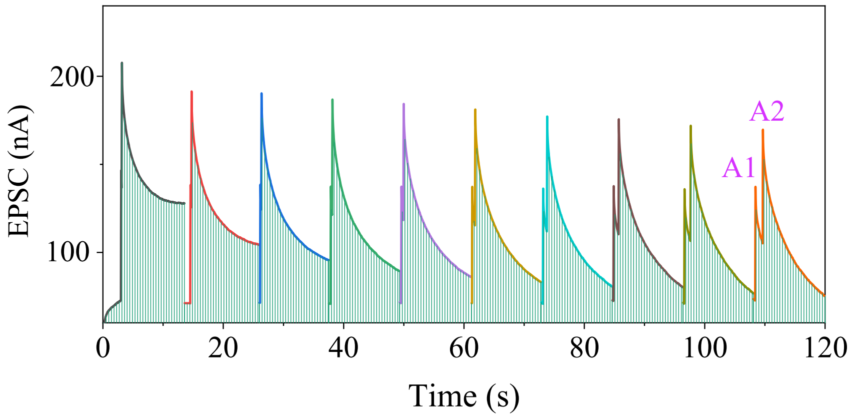

Fig. S5. EPSC peaks triggered by two successive positive spikes with increasing Δt.

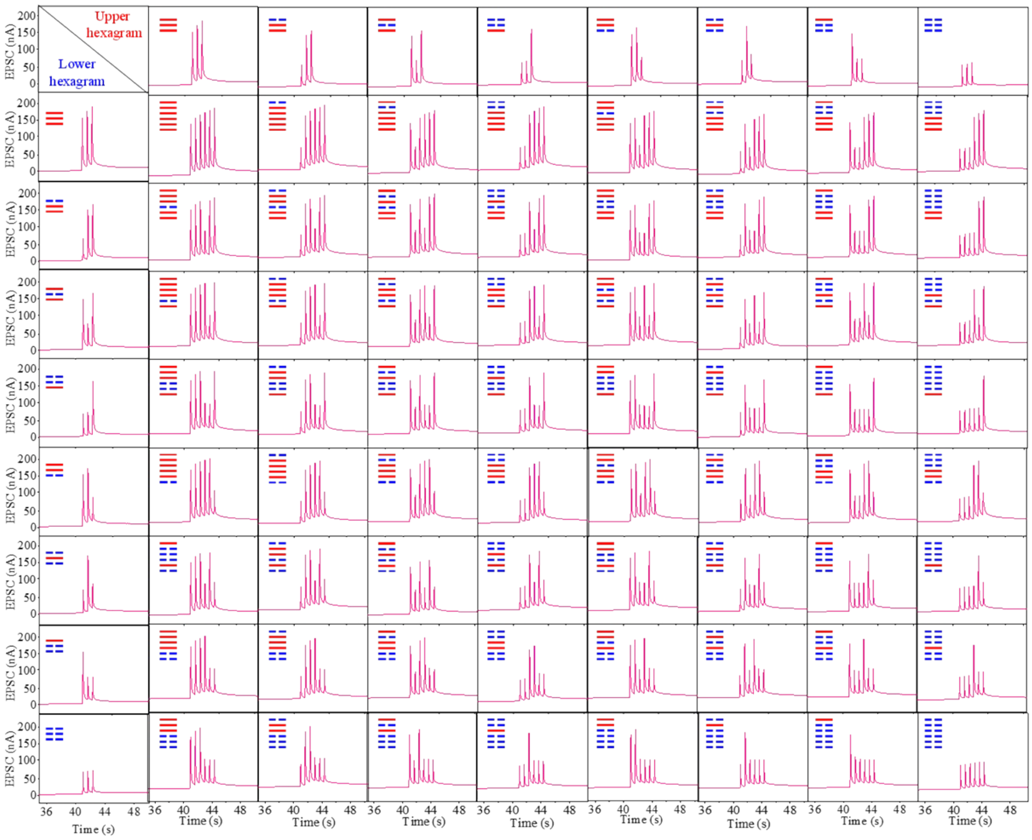

Fig. S6. 64 hexagrams in I-Ching realized by the FIST.

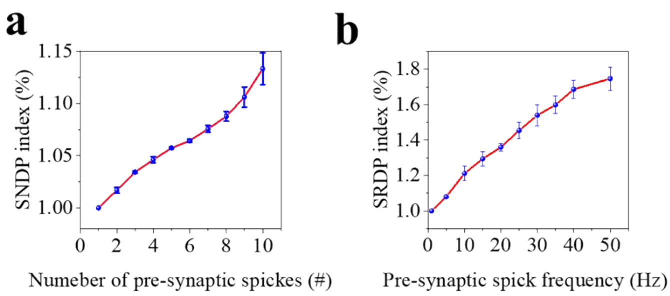

Fig. S7. (a) SNDP index (An/A1) versus spike number. (b) SRDP index versus spike frequency.

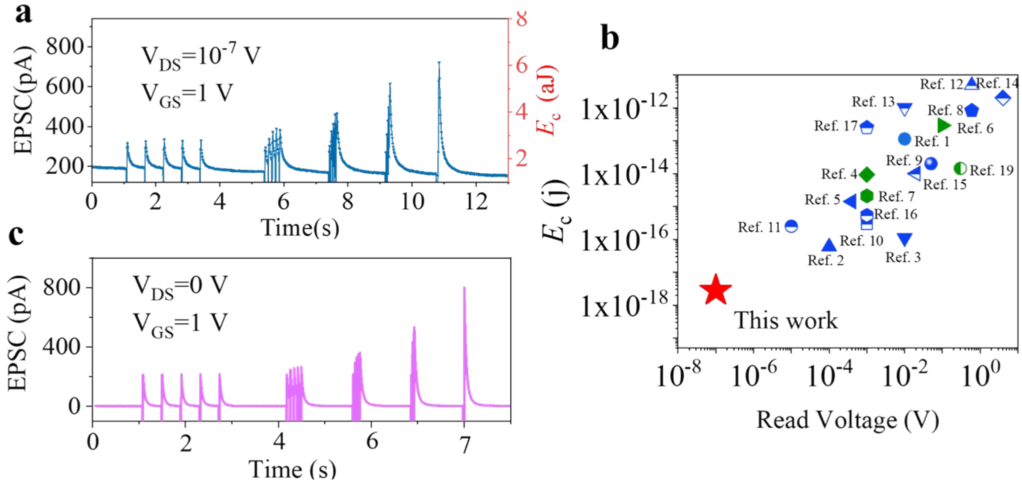

Fig. S8. (a) Variation of EPSCs and energy consumption with different spike fruqeuncy at V_{DS} =10^{-7} V. (b) Comparison of the energy consumption of this work and the previously published artificial synapses. (c) EPSC in response to five presynaptic spike trains with different frequencies at V_{DS} =0 V.[1–18]

Table S1 Comparison of the parameters between different IGZO based EDL-synaptic transistors.

Electrolyte	V_{DS} (V)	Energy consumption [J]	Year	Ref.
$Ph_3C^+BF_4^-$/PEO	10^{-7}	2.78×10^{-18}	2023	This work
Water-in-basalt	0.1	2×10^{-10}	2022	19
[EMIM][TFSI]	3	7.5×10^{-8}	2021	20
H-SiO_2	0.003	2.69×10^{-15}	2021	21
[EMIM][TFSI]	0.5	4×10^{-8}	2021	22
[EMIM][TFSI]	0.5	2.25×10^{-7}	2020	23
Na-Al_2O_3	1	$\sim10^{-7}$	2019	24
[EMIM][TFSI]	0.1	1.6×10^{-10}	2018	25
Amylose	0.2	2×10^{-7}	2017	26
KCl/H_2O	0.2	1.94×10^{-10}	2016	27
H-SiO_2	0.5	7.5×10^{-11}	2016	28
P-SiO_2	0.05	2.3×10^{-13}	2015	29

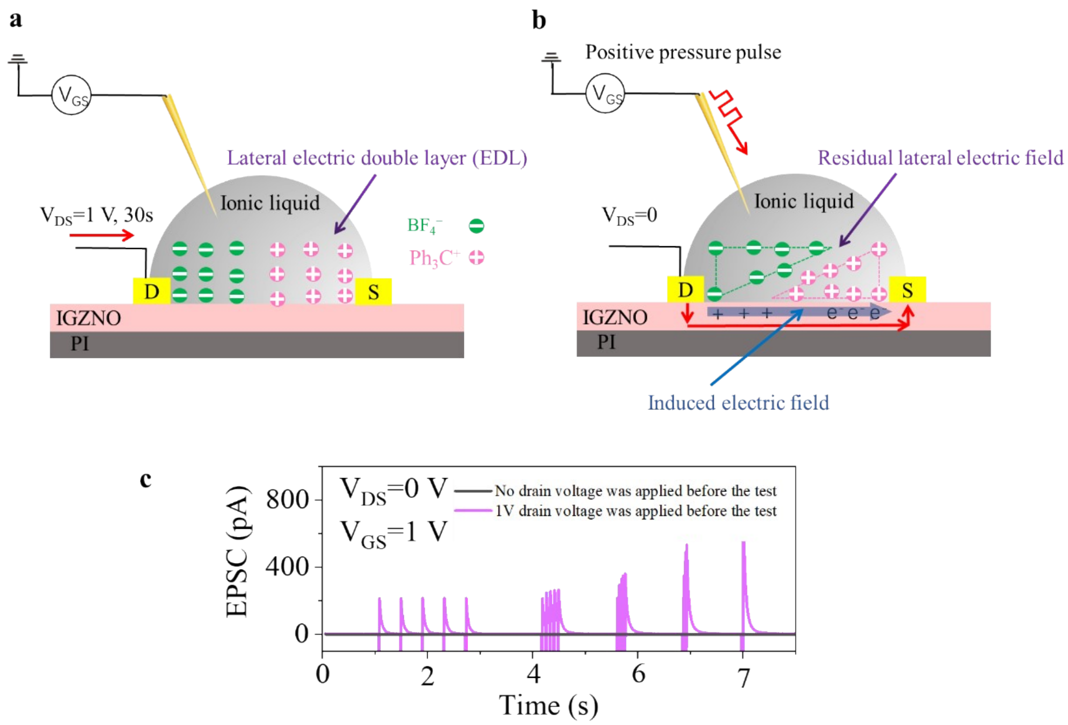

Fig. S9. (a) Schematic diagram of ion distribution in ionic liquid when V_{DS}=1 V. (b) Schematic diagram of carrier distribution within the device when a pulse is applied to the V_{GS} after the drain voltage is withdrawn. (c) Comparison of EPSCs in response to stimulation with and without pre-application of the drain voltage.

Before the “ultra-low power consumption” test, a positive voltage of 1 V is first applied to the drain electrodes for 30 s. As shown in the Fig. S8a, the cations and anions will gather around the source and drain electrode, respectively, to form lateral electric double layer (EDL) in the ionic liquid. After removing the voltage (i.e., V_{DS}=0 V), the residual lateral electric field still remained. Thus, the electron/hole will be induced at the surface of IGZNO to form another lateral electric field (Fig. S8b). When a voltage pulse is applied at the V_{GS} terminal of the IGZNO channel, it induces the generation of carriers. These generated carriers subsequently flow, driven by the internal built-in electric field within the IGZNO region. This process ultimately leads to the generation of a current. In this context, it should be noted that the internally built-in electric field within the IGZNO region is the key driving force for the directional carrier movement and current generation. In this context, the ion gel can be considered as an electrochemical capacitor that requires pre-charging to create the necessary driving force for the transport of channel carriers.

Furthermore, we performed a negative control experiment where no drain bias was applied before the " ultra-low power consumption" test. In this case, no pulse response was detected, as illustrated in Fig. S8c (black line).

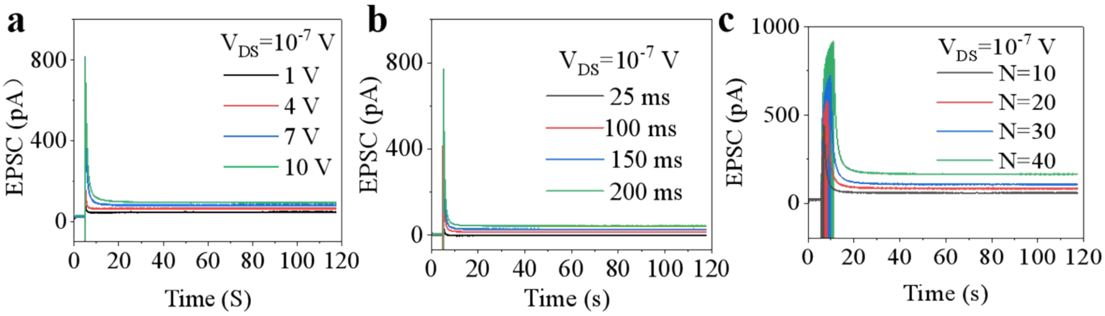

Fig. S10. The EPSC behaviors under spike stimulation with different (a) voltages, (b) durations, and (c) numbers at V_{DS} = 10^{-7} V.

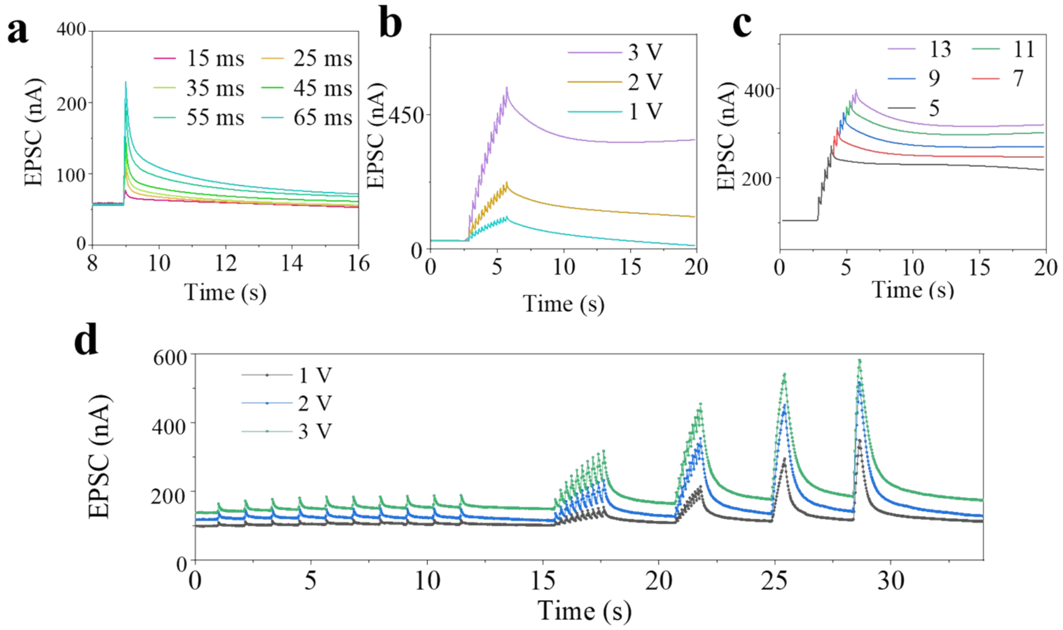

Fig. S11. The characterization of the FIST after 5-month exposure in ambient environment. (a) The EPSC behaviors under spike stimulation with different (a) durations, (b) voltages, (c) numbers, and (d) frequencies.

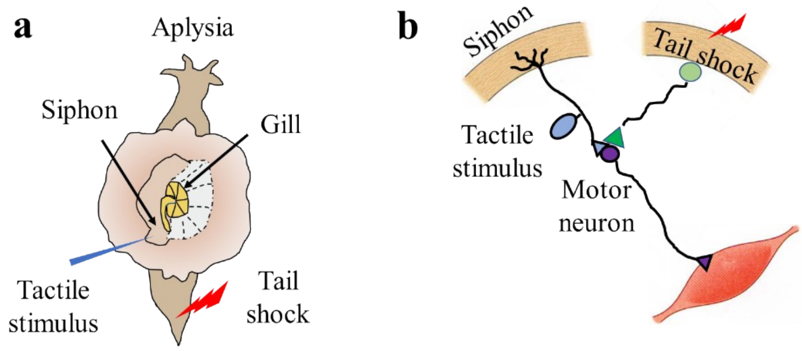

Fig. S12. (A) A dorsal view of *Aplysia* showing the gill, the animal's respiratory organ. A light touch on the siphon with a fine probe causes the siphon to contract and the gill to withdraw. Here, the mantle shelf is retracted for a better view of the gill. Sensitization of the gill-withdrawal reflex, by applying a noxious stimulus to another part of the body, such as the tail, enhances the withdrawal reflex of both the siphon and the gill. (b) The neural circuit of the *Aplysia* gill withdrawal reflex.

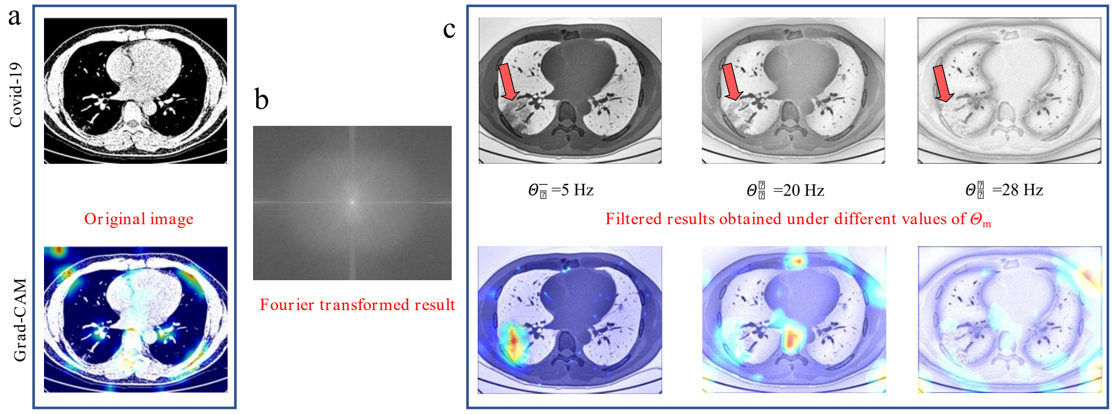

Fig. S13. The original image (a), Fourier transformed result (b), and filtered results of the Covid-19 chest CT.

This protocol implements a frequency domain filtering method using Fourier transform to enhance the edges and details in grayscale images. The input image is first transformed into the frequency domain using fft2 from numpy, producing a complex matrix fft. The function fftshift is then applied to the matrix to centralize the low-frequency signals, while moving high-frequency signals to the periphery. The Fourier transformed result (Fig. R1b) shows the frequency spectrum of the image.

A Gaussian low-pass filter H is then constructed to remove high-frequency components and smooth out the image. The strength of each pixel in H is determined based on the distance to the central pixel, which is calculated using a Gaussian function. The size of H is equal to the size of the input image.

The resulting H is multiplied with the complex matrix fft to attenuate the low-frequency signals. After applying ifftshift and ifft2 to the resulting matrix, the frequency domain filtering is completed and the filtered image is obtained. The filtered result (Fig. R1c) shows the enhanced image in which the edges and details are emphasized while low-frequency signals are suppressed. Note that the np.abs function is used to take the absolute values of the result from ifft2, resulting in intensity values between 0 and 255.

Overall, this protocol can be used to effectively enhance the edges and details in grayscale images by suppressing low-frequency signals and emphasizing high-frequency details.

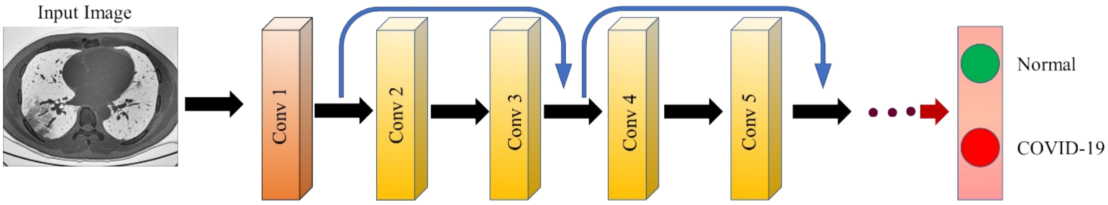

Fig. S14. The *resnet*-34 CNN were used to identify COVID-19 through chest CT. The resnet-34 consisted of one standalone convolution layer and 16 residual bocks followed by one FC layer. This network mainly overcame the degradation problem by introducing residual connections.

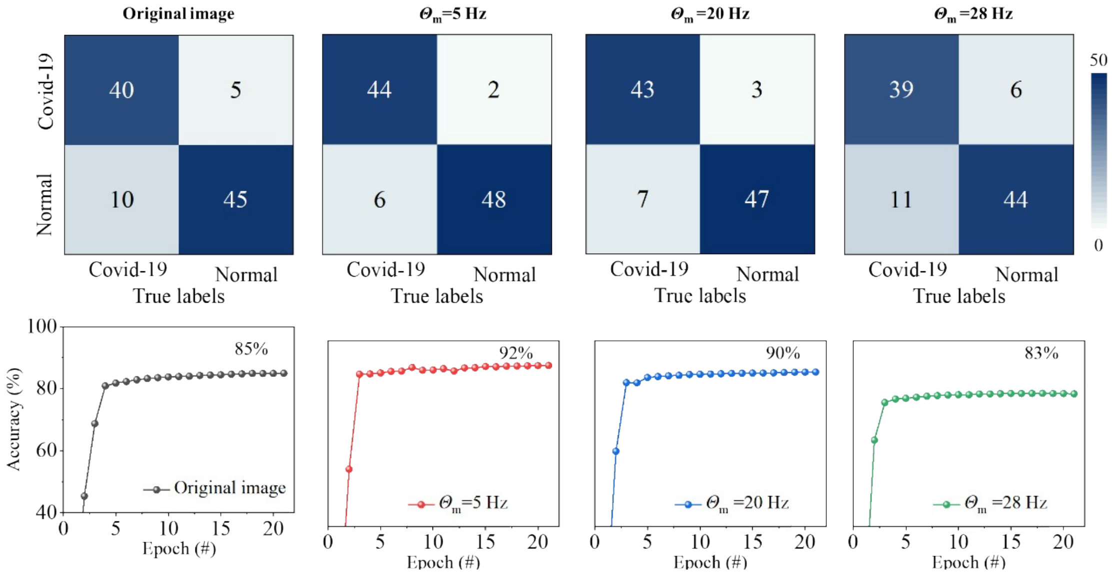

Fig. S15. Confusion matrices and corresponding accuracy plots for the resnet-34 CNN models. The COVID19-CT dataset were processed with edge detection technology at the Θ_m of 5, 20, and 28 Hz, respectively.

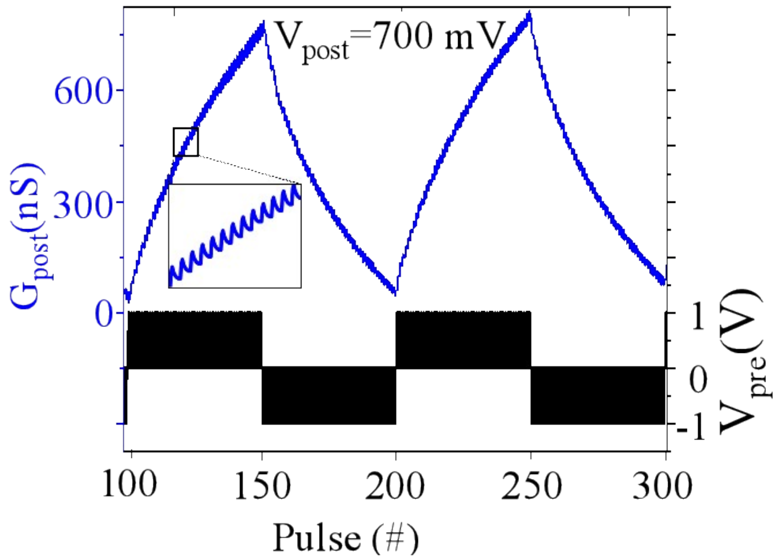

Fig. S16. LTP/D displaying 100 distinct conductance states over the operating range. The inset was a zoomed-in view to show individual states.

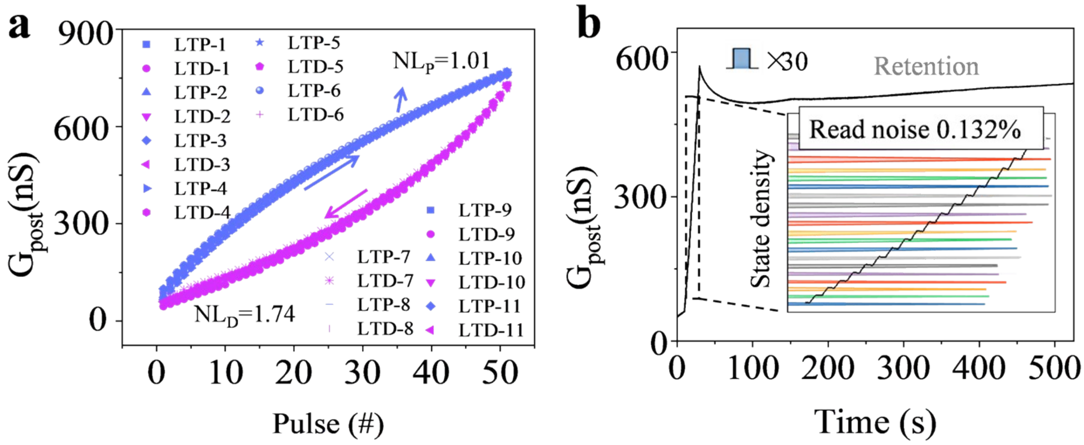

Fig. S17. (a) Nonlinearity analysis on the switching characteristics of FIST yields the maximum value of nonlinearity factors of NL_P= 1.01 and NL_D= 1.74 for G increasing and decreasing, respectively. (b) Stepwise increase in device conductance upon a series of 30 consecutive pulses. The inset shows the state density distribution of 20 states, which do not overlap, indicating extremely low read noise at 0.132% of the dynamic range.

The NL value of the LTP/D curve was calculated using the following equations:

$$G_{LTP} = B\cdot(1 - exp(- P/A_P)) + G_{min} \tag{1}$$

$$G_{LTP} =- B\cdot(1 - exp(- P/A_D)) + G_{max} \tag{2}$$

$$B = (G_{max} - G_{min})/(1 - exp(- P_{max}/A_{P,D})) \tag{3}$$

where G_{LTP} and G_{LTD} are the conductance values of the LTP and LTD regions, respectively; P is the number of applied pulses; A is a parameter representing NL; and B is a fitting constant used to normalize the conductance range. The A value was extracted from the experimental data using the MATLAB code provided as an open source[30], and the corresponding NL values were derived from tables provided by the same source.

Read noise is calculated by first grouping all sampled data by conductance level and calculating the standard deviation as follows:

$$\sigma_{level} = \sqrt{\left(\frac{\sum_{n=1}^{N}(|x - \bar{x})}{N}\right)} \tag{4}$$

where x is a conductance sample, $\bar{x}$ is the mean of the samples, and N is the number of samples.

The average read noise across the dynamic range of the device is then calculated:

$$\sigma_{level} = \frac{mean(\sigma_{level})}{G_{max} - G_{min}} \tag{5}$$

Table S2. Parameters of the FIST in comparison with other EDL or flexible artificial synapses.

Device structure: materials/substrate	Energy consumption [J]	Nonlinearity: potentiation/depression	Read noise	Ref.
Ionic gel/IGZNO/PI	2.78×10^{-18}	1.01/1.74	0.132%	This work
Ionic gel/VO_2/Mica	8.8×10^{-13}	0.026/0.045	-	[31]
$LixSiO_2$/α-Nb_2O_5/SiO_2	2×10^{-12}	1.04/2.35	2.5%	[6]
Ionic gel/GDY/MoS_2	5×10^{-15}	2.1/1.9	1.3%	[32]
Ionic gel/$LiCoO_2$	10×10^{-18}	-	11%	[33]
Ionic gel/α-MoO_3/SiO_2	6.16×10^{-12}	0.156/0.324	6.5%	[34]
Ionic gel/LixTiO/PEO	3×10^{-11}	-	1%	[35]
Ionic gel/IGZO	1.6×10^{-10}	1.75/4.5	-	[25]
Ionic gel/SIZO/PI	-	1.83/ 6.61	-	[36]
Ionic gel/P3HT/SiO_2	1.7×10^{-10}	1.25/5.72	0.5%	[37]
$CsPbBr_3$ QD/DPP-DTT/CNN	4×10^{-13}	1.5/2.5	-	[38]
Ionic gel/ZnO/SiO_2	-	3.07/2.09	-	[39]
Nafion/graphene/PMMA	1.86×10^{-15}	0.89/0.76	0.029%	[40]

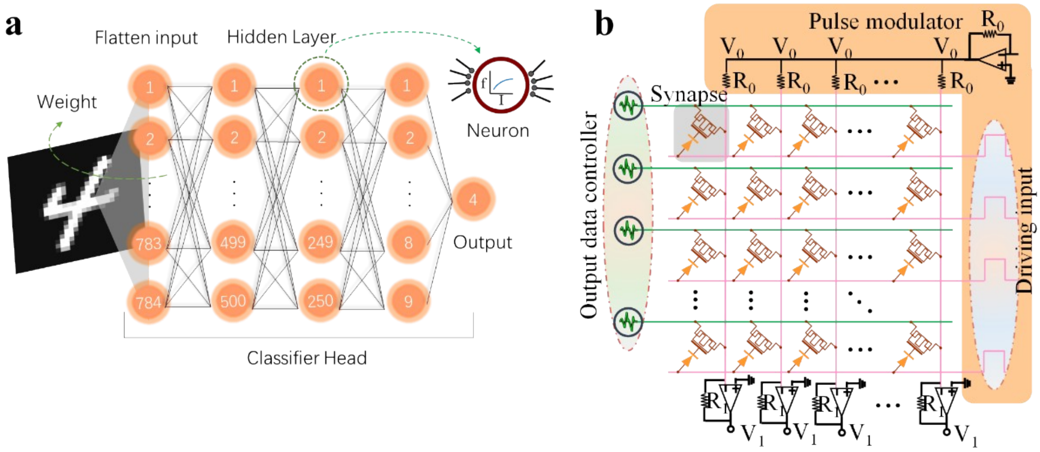

Fig. S18. (a) Schematic of ANN consisted of 784 input neurons (The input image can be divided into 28 ×28 input information for input neurons, and 10 output neurons from 0 to 9) (b) Corresponding hardware design.

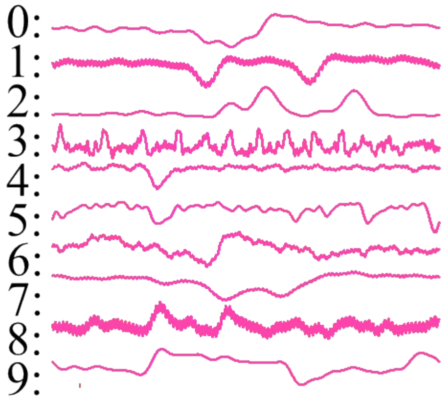

Fig. S19. EEG dataset filtered by a threshold filter (θ_m=5 Hz) to suppress noise.

Reference:

1 S. K. Lee, Y. W. Cho, J. S. Lee, Y. R. Jung, S. H. Oh, J. Y. Sun, S. B. Kim and Y. C. Joo, *Advanced Science*, 2021, **8**, 1–7.

2 G. Liu, Q. Li, W. Shi, Y. Liu, K. Liu, X. Yang, M. Shao, A. Guo, X. Huang, F. Zhang, Z. Zhao, Y. Guo and Y. Liu, *Advanced Functional Materials*, 2022, **2200959**, 1–10.

3 B. Yang, Y. Lu, D. Jiang, Z. Li, Y. Zeng, S. Zhang, Y. Ye, Z. Liu, Q. Ou, Y. Wang, S. Dai, Y. Yi and J. Huang, *Advanced Materials*, 2020, **32**, 1–12.

4 C. Ge, C. xiang Liu, Q. li Zhou, Q. hua Zhang, J. yu Du, J. kun Li, C. Wang, L. Gu, G. zhen Yang and K. juan Jin, *Advanced Materials*, 2019, **31**, 1–9.

5 L. Yin, W. Huang, R. Xiao, W. Peng, Y. Zhu, Y. Zhang, X. Pi and D. Yang, *Nano Letters*, 2020, **20**, 3378–3387.

6 Y. Li, Z. Xuan, J. Lu, Z. Wang, X. Zhang, Z. Wu, Y. Wang, H. Xu, C. Dou, Y. Kang, Q. Liu, H. Lv and D. Shang, *Advanced Functional Materials*, 2021, **31**, 1–13.

7 T. Zeng, X. Zou, Z. Wang, G. Yu, Z. Yang, H. Rong, C. Zhang, H. Xu, Y. Lin, X. Zhao, J. Ma, G. Zhu and Y. Liu, *Small*, 2021, **17**, 1–8.

8 Y. Ni, J. Feng, J. Liu, H. Yu, H. Wei, Y. Du, L. Liu, L. Sun, J. Zhou and W. Xu, *Advanced Science*, , DOI:10.1002/advs.202102036.

9 C. Eckel, J. Lenz, A. Melianas, A. Salleo and R. T. Weitz, *Nano Letters*, 2022, **22**, 973–978.

10 J. Gong, H. Yu, X. Zhou, H. Wei, M. Ma, H. Han, S. Zhang, Y. Ni, Y. Li and W. Xu, *Advanced Functional Materials*, 2020, **30**, 1–10.

11 Q. Shi, D. Liu, D. Hao, J. Zhang, L. Tian, L. Xiong and J. Huang, *Nano Energy*, 2021, **87**, 106197.

12 R. A. John, N. Tiwari, C. Yaoyi, Ankit, N. Tiwari, M. Kulkarni, A. Nirmal, A. C. Nguyen, A. Basu and N. Mathews, *ACS Nano*, 2018, **12**, 11263–11273.

13 Y. Hu, M. Dai, W. Feng, X. Zhang, F. Gao, S. Zhang, B. Tan, J. Zhang, Y. Shuai, Y. Q. Fu and P. A. Hu, *Advanced Materials*, 2021, **33**, 1–11.

14 J. Zhang, Q. Shi, R. Wang, X. Zhang, L. Li, J. Zhang, L. Tian, L. Xiong and J. Huang, *InfoMat*, 2021, **3**, 904–916.

15 L. Hu, L. Li, K. C. Chang, X. Lin, P. Huang and S. Zhang, *Advanced Functional Materials*, 2021, **31**, 1–11.

16 S. Li, M. E. Pam, Y. Li, L. Chen, Y. C. Chien, X. Fong, D. Chi and K. W. Ang, *Advanced Materials*, 2021, **2103376**, 1–12.

17 J. M. Yu, C. Lee, D. J. Kim, H. Park, J. K. Han, J. Hur, J. K. Kim, M. S. Kim, M. Seo, S. G. Im and Y. K. Choi, *Advanced Functional Materials*, 2021, **31**, 1–10.

18 C. Zhang, S. Wang, X. Zhao, Y. Yang, Y. Tong, M. Zhang, Q. Tang and Y. Liu, *Advanced Functional Materials*, 2021, **31**, 1–10.

19 H. Lee, M. Jin, H. J. Na, C. Im, J. H. Lee, J. Kim, Y. J. Gong, C. Lee, E. Lee and Y. S. Kim, *Advanced Functional Materials*, 2022, **32**, 2110591.

20 S. Kim, D. G. Roe, Y. Y. Choi, H. Woo, J. Park, J. I. Lee, Y. Choi, S. B. Jo, M. S. Kang, Y. J. Song, S. Jeong and J. H. Cho, *Science Advances*, 2021, **7**, 1–9.

21 S. I. Cho, J. B. Jeon, J. H. Kim, S. H. Lee, W. Jeong, J. Kim, G. Kim, K. M. Kim

and S. H. K. Park, *Journal of Materials Chemistry C*, 2021, **9**, 10243–10253.
22 S. Li, H. Lyu, J. Li, Y. He, X. Gao, Q. Wan, Y. Shi and L. Pan, *IEEE Electron Device Letters*, 2021, **42**, 351–354.
23 D. Choi, M. K. Song, T. Sung, S. Jang and J. Y. Kwon, *Nano Energy*, 2020, **74**, 104912.
24 S. M. Kwon, S. W. Cho, M. Kim, J. S. Heo, Y. H. Kim and S. K. Park, *Advanced Materials*, , DOI:10.1002/adma.201906433.
25 J. Sun, S. Oh, Y. Choi, S. Seo, M. J. Oh, M. Lee, W. B. Lee, P. J. Yoo, J. H. Cho and J. H. Park, *Advanced Functional Materials*, 2018, **28**, 1–9.
26 F. Shao, M. L. Cai, X. F. Gu and G. D. Wu, *Organic Electronics*, 2017, **45**, 203–208.
27 C. J. Wan, Y. H. Liu, L. Q. Zhu, P. Feng, Y. Shi and Q. Wan, *ACS Applied Materials and Interfaces*, 2016, **8**, 9762–9768.
28 F. Shao, Y. Yang, L. Q. Zhu, P. Feng and Q. Wan, *ACS Applied Materials and Interfaces*, 2016, **8**, 3050–3055.
29 F. I. E. Transistors, J. Zhou, N. Liu, L. Zhu, Y. Shi and Q. Wan, 2015, **36**, 198–200.
30 P. Chen, X. Peng and S. Yu, in Proc. 2017 IEEE International Electron Devices Meeting (IEDM), p. 6.1.1–6.1.4. (IEEE, 2017).
31 X. Deng, S. Q. Wang, Y. X. Liu, N. Zhong, Y. H. He, H. Peng, P. H. Xiang and C. G. Duan, *Advanced Functional Materials*, 2021, **31**, 1–10.
32 B. W. Yao, J. Li, X. D. Chen, M. X. Yu, Z. C. Zhang, Y. Li, T. B. Lu and J. Zhang, *Advanced Functional Materials*, , DOI:10.1002/adfm.202100069.
33 E. J. Fuller, F. El Gabaly, F. Léonard, S. Agarwal, S. J. Plimpton, R. B. Jacobs-Gedrim, C. D. James, M. J. Marinella and A. A. Talin, *Advanced Materials*, 2017, **29**, 1–8.
34 C. Sen Yang, D. S. Shang, N. Liu, E. J. Fuller, S. Agrawal, A. A. Talin, Y. Q. Li, B. G. Shen and Y. Sun, *Advanced Functional Materials*, 2018, **28**, 1–10.
35 Y. Li, E. J. Fuller, S. Asapu, S. Agarwal, T. Kurita, J. J. Yang and A. A. Talin, *ACS Applied Materials and Interfaces*, 2019, **11**, 38982–38992.
36 S. Oh, J. I. Cho, B. H. Lee, S. Seo, J. H. Lee, H. Choo, K. Heo, S. Y. Lee and J. H. Park, *Science Advances*, 2021, **7**, 1–11.
37 Y. Choi, S. Oh, C. Qian, J. H. Park and J. H. Cho, in *Nature Communications*, Springer US, 2020, vol. 11, pp. 1–9.
38 J. Zhang, T. Sun, S. Zeng, D. Hao, B. Yang, S. Dai, D. Liu, L. Xiong, C. Zhao and J. Huang, *Nano Energy*, 2022, **95**, 106987.
39 M. Jin, H. Lee, C. Im, H. J. Na, J. H. Lee, W. H. Lee, J. Han, E. Lee, J. Park and Y. S. Kim, *Advanced Functional Materials*, 2022, **32**, 2201048.
40 D. Kireev, S. Liu, H. Jin, T. Patrick Xiao, C. H. Bennett, D. Akinwande and J. A. C. Incorvia, *Nature Communications*, 2022, **13**, 4386.